Low Electronic Conductivity of $Li_7La_3Zr_2O_{12}$ (LLZO) Solid Electrolytes from First Principles

Alexander G. Squires,[1, 2] Daniel W. Davies,[3] Sunghyun Kim,[4] David O. Scanlon,[3, 5, 2] Aron Walsh,[4, 6, 2] and Benjamin J. Morgan[1, 2, *]

[1] *Department of Chemistry, University of Bath, Claverton Down BA2 7AY, United Kingdom*
[2] *The Faraday Institution, Quad One, Becquerel Avenue, Harwell Campus, Didcot, OX11 0RA, United Kingdom*
[3] *Department of Chemistry, University College London, 20 Gordon Street, London, WC1H 0AJ.*
[4] *Department of Materials, Imperial College London, Exhibition Road, London SW7 2AZ, United Kingdom*
[5] *Diamond Light Source Ltd., Diamond House, Harwell Science and Innovation Campus, Didcot, Oxfordshire OX11 0DE, United Kingdom.*
[6] *Department of Materials Science and Engineering, Yonsei University, Seoul 03722, Korea*
(Dated: July 1, 2021)

Lithium-rich garnets such as $Li_7La_3Zr_2O_{12}$ (LLZO) are promising solid electrolytes with potential application in all–solid-state batteries that use lithium-metal anodes. The practical use of garnet electrolytes, however, is limited by pervasive lithium-dendrite growth, which leads to short-circuiting and cell failure. One possible mechanism for this lithium-dendrite growth is the direct reduction of lithium ions to lithium metal within the electrolyte, and lithium garnets have suggested to be particularly susceptible to this dendrite-growth mechanism due to high electronic conductivities relative to other solid electrolytes [Han *et al.* *Nature Ener.* **4** 187, 2019]. The electronic conductivities of LLZO and other lithium-garnet solid electrolytes, however, are not yet well characterised. Here, we present a general scheme for calculating the intrinsic electronic conductivity of a nominally-insulating material under variable synthesis conditions from first principles, and apply this to the prototypical lithium-garnet LLZO. Our model predicts that under typical battery operating conditions, electron and hole mobilities are low ($<1\,cm^2\,V^{-1}\,s^{-1}$), and bulk electron and hole carrier-concentrations are negligible, irrespective of initial synthesis conditions or dopant levels. These results suggest that the bulk electronic conductivity of LLZO is not sufficiently high to cause bulk lithium-dendrite growth during cell operation, and that any non-negligible electronic conductivity in lithium garnet samples is likely due to extended defects or surface contributions.

INTRODUCTION

All–solid-state batteries that combine a solid electrolyte with a lithium-metal anode offer the potential for significantly increased energy densities compared to conventional lithium-ion batteries [1]. The development of practical solid-state batteries requires reliable solid-state electrolytes with optimised material properties [2]. The principal requirement for a practical solid-electrolyte is fast ion-conduction. As a consequence, significant research effort has been expended on developing an understanding of the physical principles that govern fast-ion transport [3–8] and on the discovery of new highly-conducting solid electrolytes [9–12]. Other material properties are also desirable for the practical use of a solid electrolyte, including good electrochemical stability over a wide voltage operating range [13], sufficient mechanical strength to impede dendrite propagation [14], and low interfacial and grain boundary resistivities [2, 15]. The development of practical solid electrolytes for use in all–solid-state batteries therefore requires a clear understanding of a broad range of relevant material properties in candidate materials, and how these properties may be controlled by tuning synthesis conditions or through targeted chemical modification [16–18].

One key property that can affect solid electrolyte performance is *electronic* conductivity. An ideal solid electrolyte should have minimal electronic conductivity to avoid gradual self-discharge [19, 20]. Non-negligible electronic conductivities have also been suggested as a possible contributing factor in lithium dendrite growth processes wherein mobile Li^+ is directly reduced to metallic Li^0 within the solid-electrolyte bulk [21–23] [24]. Recent work by Han *et al.* has shown that this "bulk" dendrite growth is more prevalent in solid electrolytes with high electronic conductivities [23], leading to the suggestion that electronic conductivity is a critical parameter that determines the degree to which a given solid electrolyte is susceptible to this dendrite nucleation and growth process. On this basis, Han *et al.* have proposed empirical upper limit thresholds for total electronic conductivity for a solid electrolyte to resist dendrite growth via this bulk nucleation mechanism of $10^{-10}\,S\,cm^{-1}$ and $10^{-12}\,S\,cm^{-1}$ at current densities of $1\,mA\,cm^{-2}$ and $10\,mA\,cm^{-2}$, respectively [23].

Despite the potential impact of non-zero electronic conductivities on the practical use of solid electrolytes

in all–solid-state batteries—particularly in cells that use lithium-metal anodes—a detailed characterisation of solid electrolyte electronic conductivities, and their dependence on factors such as synthesis conditions and sample stoichiometry, is lacking for many materials. Experimental measurements of electronic conductivities are usually performed on polycrystalline otherwise morphologically complex samples, and non-negligible electronic conductivity values are typically attributed to contributions from grain boundaries or surfaces [22, 25], with any residual bulk contributions considered to be negligible. While it may be the case that for many solid electrolytes their macroscopic electronic conductivities are dominated by "extrinsic" contributions, i.e., those arising from to surfaces and grain boundaries, it is still useful to characterise the "intrinsic" bulk electronic conductivities of solid electrolytes. As one example, if the bulk electronic conductivity is small with respect to surface and grain boundary contributions then this bulk value provides a lower limit to the net macroscopic electronic conductivity that might be obtained even under "optimal" morphological control (e.g., through sintering or surface treatment). Solid electrolytes with bulk electronic conductivities that are higher than the threshold values proposed by Hen *et al.* therefore may be fundamentally incompatible with lithium metal anodes because they are inherently susceptible to internal dendrite nucleation, irrespective of any subsequent processing [26].

The direct experimental measurement of solid electrolyte bulk electronic conductivities can be technically challenging, and has been reported for only a few cases [20]. Bulk electronic conductivities, alternatively, can be calculated entirely from first principles using schemes based on electronic structure methods. These computational models are defined in terms of relevant thermodynamic conditions, i.e., elemental chemical potentials and temperature, and net stoichiometry. First-principles models can therefore be used to map how bulk electronic conductivities vary as a function of experimental variables, such as synthesis conditions or deliberate extrinsic doping, which in turn can give insight into how experimental synthesis protocols might be optimised to limit the impact of residual bulk electronic conductivities on overall electrolyte performance.

The electronic conductivity of a semiconductor, such as a solid electrolyte, can be calculated from the products of the concentrations and mobilities of free electrons and holes, which should be determined under relevant operating conditions [27]. First principles models for calculating carrier concentrations in semiconductors under thermodynamic equilibrium are well established [28, 29], and have previously been applied to a range of battery materials [26, 30–34]. Electronic carrier mobilities for semiconductors can also be calculated from first principles; either using highly accurate but computationally costly density functional perturbation theory methods

[35–37] or more generally tractable schemes that introduce some level of approximation while remaining fully first-principles [38, 39]. These latter methods, when combined with standard methods for calculating carrier concentrations, make it practical to calculate electronic conductivities of even nominally-insulating semiconductors, such as solid electrolytes, entirely from first principles.

Here, we give a detailed description of one such computational workflow for a fully–first-principles calculation of the bulk electronic conductivity of a solid electrolyte, and demonstrate its use to calculate the electronic conductivity of the prototypical lithium garnet solid electrolyte tetragonal-$Li_7La_3Zr_2O_{12}$ (LLZO), as a function of synthesis conditions (via the component chemical potentials) and aliovalent (supervalent) doping. We find that electrons and holes in LLZO have low mobilities ($<1\,\mathrm{cm^2\,V^{-1}\,s^{-1}}$) and electronic carrier populations are vanishingly small under standard operating conditions in both undoped and doped samples. These factors suggest that the bulk electronic conductivity of LLZO is not sufficiently high to cause lithium-dendrite formation during cell operation by direct reduction of lithium ions to lithium metal within the bulk material. We therefore conclude that non-negligible electronic conductivities measured in experimental lithium garnet samples, and any associated potential for dendrite nucleation and growth, are likely due to contributions from extended defects or surfaces, and that morphological control is therefore critical to limit lithium denrite growth due to electronic conductivity.

THEORY

The electronic conductivity, σ, of a semiconductor is given by

$$\sigma = n_0 q \mu_{\mathrm{n}} + p_0 q \mu_{\mathrm{p}}, \qquad (1)$$

where n_0 and p_0 are the concentrations of free electrons and holes respectively, q is the magnitude of charge of each carrier species, and μ_{n} and μ_{p} are the electron and hole mobilities. For wide-gap materials, such as solid electrolytes, the thermal energy at room-temperature is insufficient to generate free carriers by directly exciting electrons from the valence band to the conduction band. The presence of point defects, however, can produce free charge carriers [40, 41]. Point defects exist even in nominally stoichiometric samples, due to configurational entropy, and can also be introduced by deliberate (or inadvertent) doping with extrinsic species [34, 42, 43]. Aliovalent doping of solid electrolytes is a common synthesis strategy to increase ionic conductivities through modulation of the number of ionic charge carriers [44–46]. A secondary effect of aliovalent doping, however, is to shift the position of the Fermi energy within the band gap.
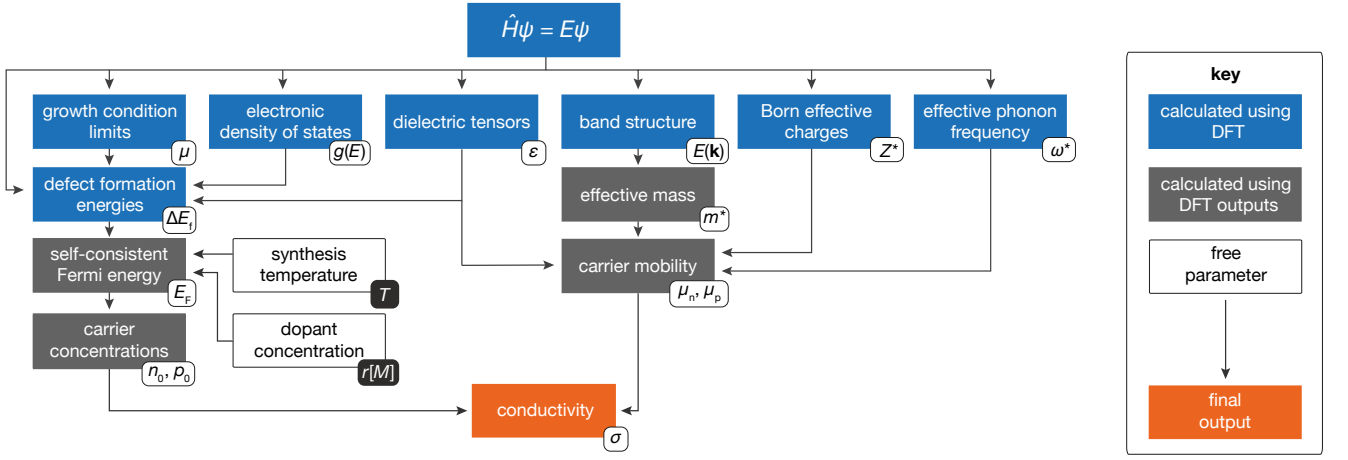
Figure 1. Schematic showing the workflow used to calculate the electronic conductivity from first-principles inputs.

Moving the Fermi energy closer to either the conduction-band or valence-band edges increases the number of thermally generated electrons or holes, respectively. Under select synthesis conditions and doping protocols, therefore, the Fermi energy can move close enough to either the valence- or conduction-band edge that the population of thermally generated electronic charge carriers is sufficiently high to give a non-negligible electronic conductivity.

Electron and hole carrier concentrations can be calculated as functions of the Fermi energy, E_F, and the bulk electronic density of states, $g(E)$;

$$n_0 = \int_0^\infty \frac{1}{e^{(E-E_F)/k_B T} + 1} g(E) \, dE, \qquad (2)$$

$$p_0 = \int_0^\infty 1 - \frac{1}{e^{(E-E_F)/k_B T} + 1} g(E) \, dE, \qquad (3)$$

where k_B is the Boltzmann constant [47]. Point defect concentrations are given by

$$[X^q] = N_0^X \exp\left(\frac{\Delta E_f^{X,q}[E_F, \Delta\mu_i]}{k_B T}\right), \qquad (4)$$

where N_0^X is the density of available sites for defect X, $\Delta E_f^{X,q}$ is the formation energy of defect X in charge-state q, which in turn depends on the Fermi energy, E_F, and $\Delta\mu_i$ are the chemical potentials of any atomic species added to or removed from the system when forming each defect [27, 48]. Equations 2, 3, and 4 are coupled by a common Fermi energy, which itself is constrained by the requirement that the system is net charge-neutral—the charge-density contributions from electrons, holes, and any charged point-defects must sum to zero;

$$\rho(E_F) = \sum_{X^q} q[X^q] + p_0 - n_0 = 0. \qquad (5)$$

Calculating equilibrium carrier concentrations under specific synthesis conditions—which define the external chemical potentials—consists of finding a self-consistent solution to Equations 2, 3, and 4, subject to the charge-neutrality constraint expressed in Equation 5 [27, 29].

The effect of extrinsic dopants can be accounted for by including an additional term in Equation 5 [29, 34, 43]. For a dopant M with relative charge r and fixed concentration $[M^r]$, ρ becomes

$$\rho(E_F, r[M^r]) = \sum_{X^q} q[X^q] + p_0 - n_0 + r[M^r]. \qquad (6)$$

In the dilute-defect limit there is no direct interaction between dopants and native defects, and the doping response does not depend explicitly on the choice of dopant species and insertion site but only on the product $r[M^r]$.

The necessary inputs to solve Equations 2—6 are the reference elemental chemical potentials, which are restricted by the condition that the defect host material must be thermodynamically stable with respect to likely degradation products; the native defect formation energies; the dielectric tensor for the material, which is used to correct for spurious implicit interactions between defects and their periodic images during formation energy calculations [49]; and the electronic density of states for the non-defective system. These parameters can all be obtained using first-principles methods such as Density Functional Theory (DFT) [28, 50]. The mobilities of the electron and hole charge carriers—μ_n and μ_p, respectively—can be calculated using the Feynman variational solution for Fröhlich's polaron Hamiltonian and integrating the polaron-response function to obtain a mobility [51, 52]. This method for calculating polaron mobilities assumes that charge-carrier mobilities are limited by scattering by optical phonon modes, which is the dominant factor for heteropolar crystals [53]. Because the approach used here to calculating carrier mobilities considers only one scattering process and one source of electron–phonon coupling, we obtain an upper limit value for the carrier mobilities in a perfect crystal. The in-

puts for this calculation are the dielectric constant of the solid electrolyte, Born effective charges, a characteristic phonon frequency and charge-carrier effective masses: again, these are all calculable using first-principles methods [54].

We have used this theoretical framework, illustrated schematically in Fig. 1, to calculate the bulk electronic conductivity of LLZO. All calculations were performed on the low-temperature tetragonal phase of LLZO, as opposed to the high–ionic-conductivity high-temperature cubic phase. A key component of our model is the accurate calculation of self-consistent point-defect populations. The high-temperature cubic phase of LLZO has highly mobile lithium ions and high intrinsic lithium disorder. This violates the assumptions used in the derivation of Eqn. 4, which is formally valid only for systems with an ordered ground-state [34]. Rather than introduce unquantified errors—by assuming Eqn. 4 holds for an inherently disordered system—we instead consider the low-temperature lithium-ordered LLZO phase and assume that the structural similarity between the ordered and disordered LLZO phases—excepting the degree of lithium disorder—means our results provide at least an order-of-magnitude estimate of the electronic conductivity in practical lithium-garnet solid electrolytes.

RESULTS

Carrier Mobilities. The electronic conductivity is given by the products of carrier concentrations and carrier mobilities, summed over contributions from both electron and hole carriers (Eqn. 1). For the carrier mobilities, we are interested in these values under typical cell operating conditions, which we take as 298 K. Our model assumes that the carrier mobilities do not vary with changes in synthesis conditions or doping levels. The carrier mobilities therefore act as fixed scaling factors that can be used to convert carrier concentrations—which do vary according to synthesis conditions and doping levels—into electronic conductivities.

To solve Fröhlich's polaron model, we first determine the electron and hole effective masses. Carrier populations in wide-gap insulators such as LLZO are low compared to conventional semiconductors, and we therefore calculate "curvature" effective-masses at the conduction band minimum (CBM) and valence band maximum (VBM) [55]. The band-structure for t-LLZO is shown in Fig. 2, and the resulting curvature effective masses are given in Table I. The lowest effective mass found for charge carriers in LLZO at the band edges is $2.35\,m_{\mathrm{e}}$ [56]. Using these data to calculate room-temperature carrier mobilities yields a maximum value (considering both electron and hole mobilities) of $0.2\,\mathrm{cm^2\,V^{-1}\,s^{-1}}$ [57]

Carrier Concentrations. The electron and hole carrier populations are given by Eqns. 2 and 3, which
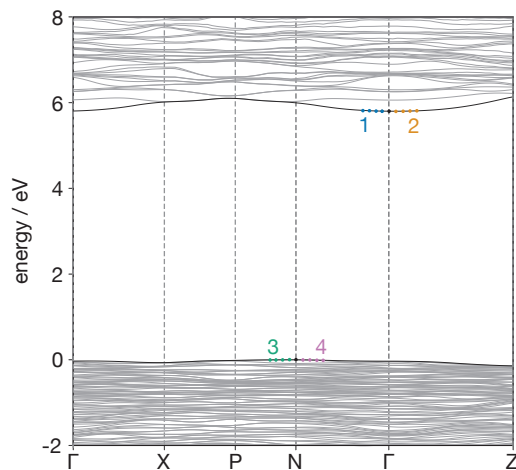

Figure 2. The electronic band structure of t-LLZO calculated using HSE06, plotted along a high symmetry path in the Brillouin zone according to the Bradley and Cracknell notation [58]. The coloured points mark the band edges used to calculate the effective masses, with numeric labels indicating the corresponding entry in Table I.

Carrier	Direction	m^*	No.
electron	$\Gamma \longrightarrow N$	2.35	1
electron	$\Gamma \longrightarrow Z$	2.41	2
hole	$N \longrightarrow P$	2.39	3
hole	$N \longrightarrow \Gamma$	21.44	4

Table I. Curvature effective masses, m^*, for holes and electrons determined by a parabolic fit to LLZO band edges [59], and the relevant crystallographic direction for transport. Numbers indicate the corresponding features in the electronic band structure (Fig. 2).

are solved self-consistently along with Eqn. 4 (which describes point-defect concentrations) under the constraint of net charge-neutrality (Eqns. 5 or 6). This self-consistent calculation requires specifying the thermodynamic conditions, i.e. defining the temperature, which appears in Eqns. 2 and 4; and the reference elemental chemical potentials, which affect the defect formation energies (Eqn. 4). While our model treats the elemental chemical potentials as free parameters, in our analysis we restrict this chemical potential space to values that are, in principle, experimentally accessible; we consider only sets of chemical potentials for which LLZO is thermodynamically stable with respect to competing phases [34, 60]. The predicted region of thermodynamic stability of LLZO spans a range of values in four-dimensional $\{\Delta\mu_{\mathrm{Li}}, \Delta\mu_{\mathrm{O}}, \Delta\mu_{\mathrm{La}}, \Delta\mu_{\mathrm{Zr}}\}$ chemical-potential space that can be broadly characterised along an O-rich/metal-poor→O-poor/metal-rich axis. To further restrict this region to values corresponding to typical synthesis conditions, we relate the oxygen chemical potential to the
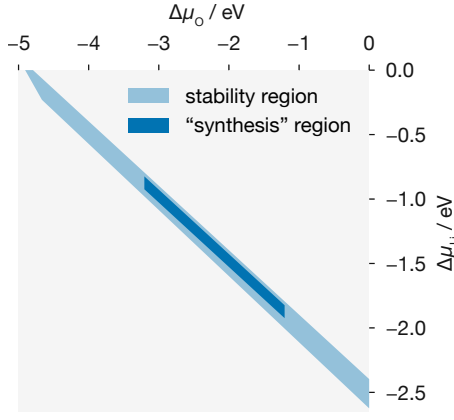
Figure 3. Chemical potential stability region of LLZO in the $\{\Delta\mu_{\mathrm{Li}}, \Delta\mu_{\mathrm{O}}\}$ plane. The dark blue region is constricted by Equation 7 to represent synthesis conditions ranging from $T = 1000\,\mathrm{K}$ to $1500\,\mathrm{K}$ and $P_{\mathrm{O}_2} = 1\,\mathrm{atm}$ to $1 \times 10^{-10}\,\mathrm{atm}$.

synthesis pressure, P, and temperature, T, via

$$\Delta\mu_{\mathrm{O}}(T,P) = \frac{1}{2}\Bigg\{(T - T_0) \tag{7}$$
$$-T\left[S_0 + C_p \ln\frac{T}{T_0} + k_{\mathrm{B}} \ln\frac{P}{P_0}\right]\Bigg\},$$

using the experimental value for the oxygen standard entropy, $S_0 = 205\,\mathrm{J\,mol^{-1}\,K^{-1}}$ [61]. Assuming oxygen behaves as an ideal gas, we use $C_p = (7/2)\,k_{\mathrm{B}}$ for the constant-pressure specific–heat-capacity per diatomic molecule. This reproduces well experimentally tabulated values of $\Delta\mu_{\mathrm{O}}(T,P)$, with a maximum error of $\sim 15\,\mathrm{meV}$ at the higher end of the temperature range under which LLZO is typically synthesised ($1500\,\mathrm{K}$) [62, 63]. The full thermodynamic-stability region of LLZO is limited by the additional constraints we place on the oxygen chemical potential, corresponding to synthesis temperatures of $1000\,\mathrm{K}$ to $1500\,\mathrm{K}$, and oxygen partial pressures of $1\,\mathrm{atm}$ to $1 \times 10^{-10}\,\mathrm{atm}$. The reduced synthetically accessible chemical potential volume is plotted in the $\{\Delta\mu_{\mathrm{Li}}, \Delta\mu_{\mathrm{O}}\}$ plane in Fig. 3.

While LLZO is typically synthesised at high temperature (up to $1500\,\mathrm{K}$), we are ultimately interested in predicting the electronic conductivity at much lower temperatures corresponding to typical operating conditions—approximately $298\,\mathrm{K}$. We assume that host-framework point-defects, i.e. those involving La, Zr, or O, formed during synthesis are "frozen in" during subsequent cooling to operating temperatures. The kinetic barriers for the reorganization of such defects within the host-framework are large, which prevents the system from fully re-equilibrating at low temperatures on experimentally relevant timescales [64]. Because LLZO is a fast-ion solid electrolyte, with highly-mobile lithium interstitials and vacancies, we do, however, expect V_{Li} and Li_{i} defects to re-equilibrate during cooling. Electron and hole

populations are similarly expected to re-equilibrate on experimentally-relevant timescales [33, 65].

To obtain electron and hole carrier concentrations under operating conditions, as a function of initial synthesis conditions, we therefore first calculate self-consistent defect and charge-carrier concentrations for the relevant range of elemental chemical potentials at a characteristic synthesis temperature of $1500\,\mathrm{K}$. We then fix the concentrations of all defects, except for V_{Li} and Li_{i}, and recompute pseudo-equilibrium defect and charge-carrier populations at a range of lower temperatures to predict how carrier concentrations change during sample cooling. For this second calculation, we impose the constraint that there is no lithium exchange with the surroundings during cooling, i.e., the net lithium stoichiometry is set by the high-temperature synthesis conditions.

To illustrate the effect of varying synthesis conditions on the resulting carrier concentrations, we consider six chemical potential "limits", which correspond to the vertices of the estimated synthetically-accessible chemical-potential space (Fig. 3). These chemical-potential limits can be considered as two groups depending on whether they can be broadly characterised as O-rich/metal-poor or O-poor/metal-rich. Fig. 4 shows the calculated pseudo-equilibrium electron and hole carrier-concentrations as a function of the re-equilibration temperature, for each of these limits. For each set of synthesis conditions (elemental chemical potentials) we present data for undoped LLZO, with only intrinsic defects present, as well as for aliovalently-doped LLZO, where we introduce a concentration of 0.15 per formula unit of a generic supervalent dopant with relative charge $r = +2$—this models the effect of supervalent dopants such as a M^{3+} dopant occupying a lithium site, i.e. $M_{\mathrm{Li}}^{\bullet\bullet}$ (see Equation 6) [63, 66, 67]. Defect transition level diagrams and respective self-consistently calculated Fermi energies are plotted in Fig. S1.

Under O-rich/metal-poor conditions (Fig. 4; top panels) we predict p-type conductivity, but this can become slightly n-type when the system is cooled. In contrast, under O-poor/metal-rich conditions (Fig. 4; bottom panels), we predict strong n-type behaviour. The total number of charge carriers (summing both electrons and holes) under O-rich/metal-poor conditions, however, is smaller than under O-poor/metal-rich conditions. These low carrier concentrations are associated with a "mid-gap" Fermi energy: within the considered chemical potential space, the minimum calculated Fermi energy is $2.67\,\mathrm{eV}$, and the maximum calculated Fermi energy is $3.78\,\mathrm{eV}$; the calculated band gap, aligned to the valence band maximum, ranges from $0\,\mathrm{eV}$ to $5.9\,\mathrm{eV}$. Ultimately, we predict low carrier concentrations under all synthesis conditions and doping protocols.

Electronic Conductivities. The results above predict that under all considered synthesis conditions, carrier concentrations are relatively high at the initial synthesis
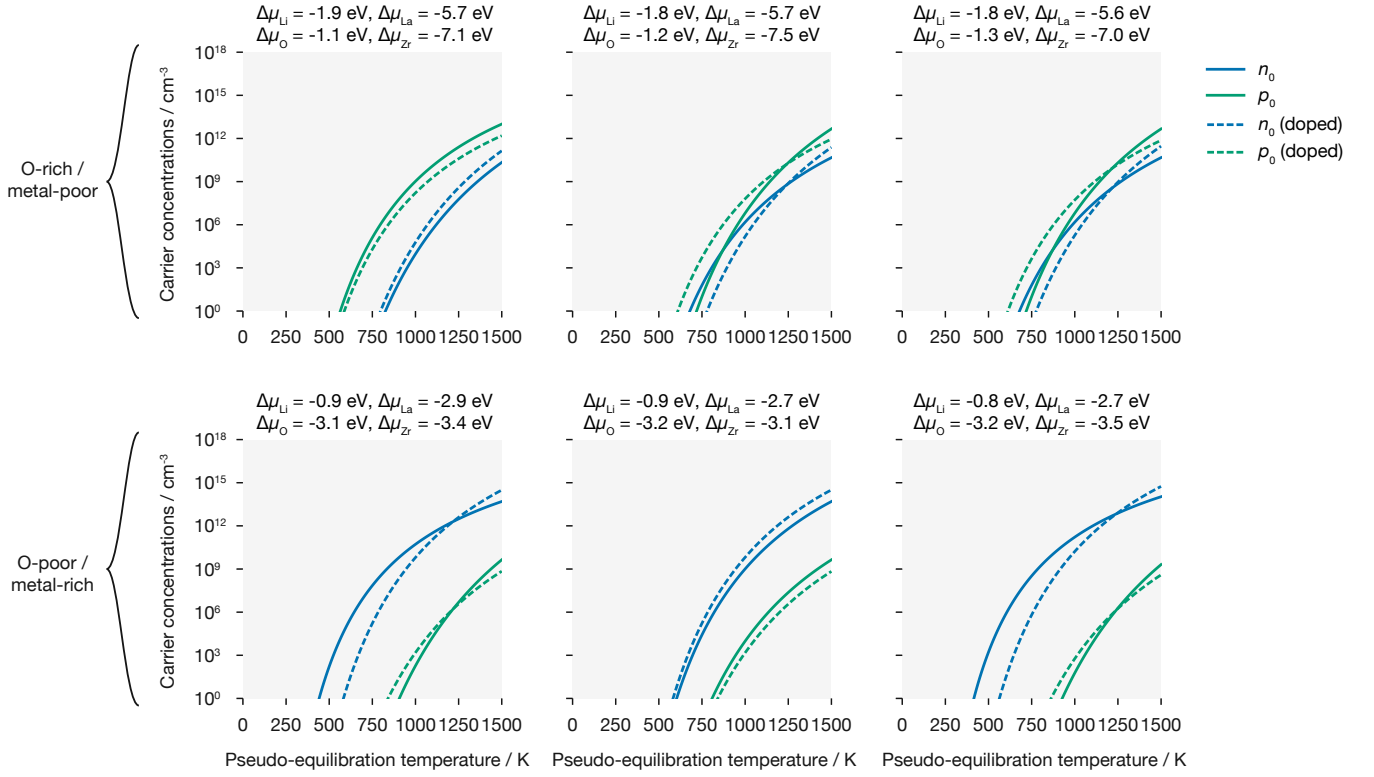
Figure 4. n- and p-type carrier concentrations at six sets of chemical potentials (each set corresponds to a vertex of the estimated chemical potential stability region that LLZO can be synthesised within). The chemical potentials used to calculate defect concentrations are shown above each plot. The carrier concentrations are calculated at 1500 K initially, the concentrations of all defects other than lithium vacancies, interstitials and electron and hole concentrations are then fixed to these high temperature values for subsequent, lower temperature solutions. All carrier concentrations are given for both a undoped sample, and a sample containing 0.15 per formula unit of some dopant M^{2+}.

temperature of 1500 K, but decrease by many orders of magnitude as the temperature is reduced under pseudo-equilibrium conditions. The significance of this decrease in carrier concentrations can be seen more clearly by plotting approximate electronic conductivities (via Eqn. 1) by scaling these predicted carrier concentrations by the previously calculated maximum room-temperature carrier mobility of $0.2 \, \mathrm{cm^2 \, V^{-1} \, s^{-1}}$. The resulting "room-temperature" intrinsic (undoped) and extrinsic (doped) electronic conductivities are plotted in Fig. 5 for both O-rich/metal-poor and O-poor/metal-rich conditions, as a function of the temperature at which the $\mathrm{e^-/h^{\bullet}}$ and $V_{\mathrm{Li}}/\mathrm{Li_i}$ populations re-equilibrate. In both cases, the high carrier concentrations for as-synthesised samples (1500 K) correspond to room-temperature electronic conductivities well in excess of the threshold values proposed by Han *et al.* For these high bulk electronic conductivities to be observed under operating conditions, however, would require that the electron and hole carrier populations do not re-equilibrate during, or after, sample cooling. Re-equilibration of the electron and hole carrier populations (and the lithium vacancy and interstitial populations), however, greatly reduces the carrier concentra-

tions (Fig. 4) and the corresponding room-temperature electronic conductivities are predicted to be well below the threshold values proposed for intrinsic bulk lithium-dendrite growth.

SUMMARY AND DISCUSSION

Minimising the electronic conductivity of lithium solid electrolytes is crucial to the effective operation of a solid state battery. In recent years. non-negligible electronic conductivity has been linked to lithium-dendrite growth in lithium solid electrolytes, leading to cell failure. [21, 23] This raises the question of whether the intrinsic electronic conductivity of various solid state electrolytes makes them fundamentally incompatible with a lithium metal anode. Motivated by this proposal, and to provide an estimate of the room-temperature bulk electronic conductivities of lithium-garnet solid electrolytes, we presented a general fully–first-principles scheme for calculating bulk electronic conductivities of wide-gap semiconductors, and have applied this to calculate the electronic conductivity of the lithium-conducting solid electrolyte LLZO, as a function of synthesis conditions and doping
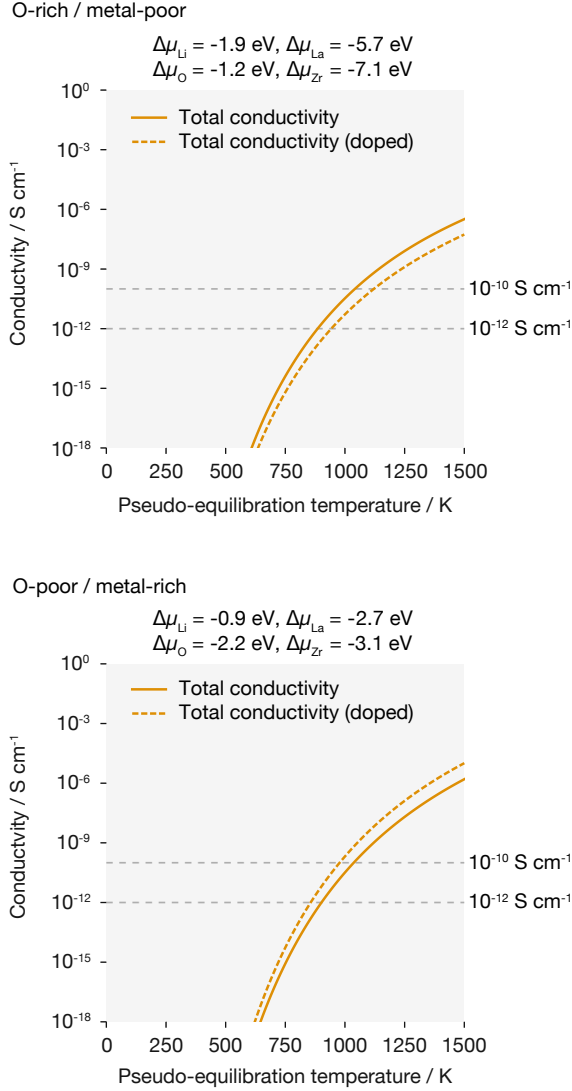
O-rich / metal-poor

$\Delta\mu_{Li}$ = -1.9 eV, $\Delta\mu_{La}$ = -5.7 eV
$\Delta\mu_O$ = -1.2 eV, $\Delta\mu_{Zr}$ = -7.1 eV

O-poor / metal-rich

$\Delta\mu_{Li}$ = -0.9 eV, $\Delta\mu_{La}$ = -2.7 eV
$\Delta\mu_O$ = -2.2 eV, $\Delta\mu_{Zr}$ = -3.1 eV

Figure 5. Effective "room temperature" (298 K) electronic conductivities for LLZO synthesised under O-rich/metal-poor (top panel) and O-poor/metal-rich (bottom panel) conditions, as a function of $\{V_{Li}, Li_i\}$ and $\{e^-/h^\bullet\}$ pseudo-equilibration temperature. Conductivities are calculated via Eqn. 1), using the electronic carrier concentrations in Fig. 4 and the previously calculated maximum room-temperature electron and hole carrier mobilities of $0.2\,cm^2\,V^{-1}\,s^{-1}$. Solid lines show results for undoped LLZO, and dashed lines show results under supervalent doping with M^{2+} at a concentration of 0.15 per formula unit.

protocol.

We find that electronic carriers have low mobilities $(<1\,cm^2\,V^{-1}\,s^{-1})$ owing to large hole and electron effective masses and strong electron–phonon interactions. While the electronic carrier populations predicted under typical synthesis conditions ($\sim$1500 K) are sufficiently high that the corresponding room-temperature electronic conductivities would be well in excess of the threshold values proposed by Han *et al.*, these electronic car-

rier populations decrease significantly under subsequent sample cooling. At room-temperature, assuming full re-equilibration of $e^-/h^\bullet$ carriers (and V_{Li}/Li_i defects), carrier concentrations are predicted to be negligible, giving room-temperature electronic conductivities that are well below the threshold values of Han *et al.* This result is consistent with recent experimental data that gave a much lower electronic conductivity for single-crystal samples of LLZO than previously reported for polycrystalline samples [20]. We note, however, that in experimental samples there may be additional contributions to electronic conductivity from electronic charge carriers that are thermally excited at high temperature (e.g., directly after synthesis) and then kinetically trapped during cooling, to give non-equilibrium carrier populations with higher electronic conductivities than we predict here.

In the context of understanding the possible contribution of electronic conductivity to dendrite nucleation and growth, one limitation of the present study is that it considers only *bulk* properties. Real-world solid electrolytes possess surfaces and (typically) grain boundary interfaces, which may contribute to net electronic conductivities or otherwise promote lithium-dendrite growth. Previous theoretical work has observed dramatic band-gap reductions at LLZO surfaces ($E_g^{bulk} = 5.46\,eV$, $E_g^{surface} = 2.19\,eV$) [25] and a recent combined experimental and theoretical study predicts similar narrowing at grain boundaries ($E_g^{bulk} = 6\,eV$, $E_g^{gb} = 1\,eV$ to $3\,eV$)[68]. Such band-gap narrowing is expected to greatly increase the number of free charge-carriers at thermal equilibrium, potentially giving high local electronic conductivities that may facilitate dendrite nucleation and growth. Grain boundaries and surfaces may also exhibit non-bulk defect populations. Local variations in defect standard chemical potentials can drive defect segregation to (or from) these regions, causing local shifts in the electrostatic potential (band bending) and increasing (or decreasing) local free carrier populations relative to the bulk [69, 70]. Lithium nucleation has been observed at grain boundaries in LLZO in recent experimental studies [22, 68], which illustrates the likely critical role of sample morphology on dendrite growth in lithium garnets, and underscores the need for the development of new theoretical methods that can accurately model equilibrium defect and free carrier populations at interfaces, such as grain boundaries and surfaces.

COMPUTATIONAL METHODS AND DATA ACCESS

We have used DFT data taken from our previous study of the intrinsic defect chemistry of tetragonal LLZO [34], which are available as Ref. 71. Scripts used to generate Figs. 2–5 are available at Ref. 72,

and the raw data is available at Ref. 73. This analysis relies on several open-source Python packages, including PYMATGEN [74], MATPLOTLIB [75], PANDAS [76], NUMPY [77], SCIPY [78] PHONOPY-SPECTROSCOPY [79] VASPPY [80, 81], TQDM [82], EFFMASS [59], and the Julia package POLARONMOBILITY.JL.[38] The code used to model defect and carrier concentrations is available at Ref. [83] a Python implementation of the Fortran code SC-Fermi.[29]

All DFT data used in this study have been computed using the plane-wave DFT code VASP [84–86]. Interactions between core and valence electrons are described using pseudopotentials within the projector-augmented wave (PAW) method [87]. Unless otherwise noted, all calculations used the hybrid-DFT functional HSE06 [88, 89] and utilised a plane wave energy cutoff of $520\,\mathrm{eV}$; optimised lattice parameters were obtained by performing a series of constant-volume geometry optimisation calculations, and fitting the resulting energy–volume data to the Murnaghan equation of state [90]. k-point sampling was selected to ensure energies converged to $<1\,\mathrm{meV/atom}$: all LLZO calculations used a $2 \times 2 \times 2$ Monkhorst-Pack k-point mesh. k-point sampling for competing phases and elemental reference calculations is described in the supporting dataset.[73]

The high-frequency dielectric function was calculated using the method of Gajdoš *et al.* [91], while the ionic response was calculated using Density Functional Perturbation Theory using the PBEsol GGA functional [92]. Effective masses are calculated from fitting to the LLZO band structure, calculated non–self-consistently using the charge density data computed during a single-point electronic structure calculation following geometry optimisation.

We use the supercell approach for calculating defect formation energies [28, 50]. The defects considered in our study are: lithium vacancies and interstitials, V_{Li} and $\mathrm{Li_i}$; oxygen vacancies and interstitials, V_{O} and $\mathrm{O_i}$; holes on framework oxygen $\mathrm{O_O^{\bullet}}$, lanthanum and zirconium vacancies, V_{La} and V_{Zr}; zirconium interstitials, $\mathrm{Zr_i}$; and cation anti-sites $\mathrm{La_{Zr}}$, $\mathrm{Zr_{Li}^{oct}}$, $\mathrm{Zr_{Li}^{tet}}$, $\mathrm{Zr_{La}}$, $\mathrm{Li_{La}}$, $\mathrm{La_{Li}^{oct}}$ and $\mathrm{Li_{Zr}}$ – a superscript oct or tet denotes a defect located at an octahedral or tetrahedral Li site, respectively. Structural relaxations for all defects were calculated with cell parameters fixed to the optimised values for stoichiometric LLZO. Electrostatic potentials of the bulk and defective calculations were aligned via the difference in spatially averaged electrostatic potentials in the two simulation cells. For this study, we have used the image charge correction scheme of Lany and Zunger [49], adapted for anisotropic systems by Murphy and Hine [93].

---

* b.j.morgan@bath.ac.uk

[1] Q. Zhao, S. Stalin, C.-Z. Zhao, and L. A. Archer, Designing solid-state electrolytes for safe, energy-dense batteries, Nat. Rev. Mater. **5**, 229 (2020).

[2] T. Famprikis, P. Canepa, J. A. Dawson, M. S. Islam, and C. Masquelier, Fundamentals of inorganic solid-state electrolytes for batteries, Nature Mater. **21**, 1 (2019).

[3] M. Burbano, D. Carlier, F. Boucher, B. J. Morgan, and M. Salanne, Sparse cyclic excitations explain the low ionic conductivity of stoichiometric $\mathrm{Li_7La_3Zr_2O_{12}}$, Phys. Rev. Lett. **116**, 135901 (2016).

[4] X. He, Y. Zhu, and Y. Mo, Origin of fast ion diffusion in super-ionic conductors, Nature Comm. **8**, 15893 (2017).

[5] M. A. Kraft, S. P. Culver, M. Calderon, F. Böcher, T. Krauskopf, A. Senyshyn, C. Dietrich, A. Zevalkink, J. Janek, and W. G. Zeier, Influence of lattice polarizability on the ionic conductivity in the lithium superionic argyrodites $\mathrm{Li_6PS_5}X$ (X = Cl, Br, I), J. Am. Chem. Soc. **139**, 10909 (2017).

[6] D. D. Stefano, A. Miglio, K. Robeyns, Y. Filinchuk, M. Lechartier, A. Senyshyn, H. Ishida, S. Spannenberger, D. Prutsch, S. Lunghammer, D. Rettenwander, M. Wilkening, B. Roling, Y. Kato, and G. Hautier, Superionic diffusion through frustrated energy landscape, Chem **5**, 2450 (2019).

[7] S. P. Culver, A. G. Squires, N. Minafra, C. W. F. Armstrong, T. Krauskopf, F. Böcher, C. Li, B. J. Morgan, and W. G. Zeier, Evidence for a solid-electrolyte inductive effect in the superionic conductor $\mathrm{Li_{10}Ge_{1-x}Sn_xP_2S_{12}}$, J. Amer. Chem. Soc. **142**, 21210 (2020).

[8] B. J. Morgan, Mechanistic origin of superionic lithium diffusion in anion-disordered $\mathrm{Li_6PS_5}X$ argyrodites, Chem. Mater. **33**, 2004 (2021).

[9] Y. Zhang, X. He, Z. Chen, Q. Bai, A. M. Nolan, C. A. Roberts, D. Banerjee, T. Matsunaga, Y. Mo, and C. Ling, Unsupervised discovery of solid-state lithium ion conductors, Nature Comm. **10**, 1 (2019).

[10] L. Kahle, A. Marcolongo, and N. Marzari, High-throughput computational screening for solid-state Li-ion conductors, Energy Environ. Sci. **13**, 928 (2020).

[11] S. Muy, J. Voss, R. Schlem, R. Koerver, S. J. Sedlmaier, F. Maglia, P. Lamp, W. G. Zeier, and Y. Shao-Horn, High-throughput screening of solid-state Li-ion conductors using lattice-dynamics descriptors, ISCIENCE **16**,

270 (2019).

[12] A. D. Sendek, E. D. Cubuk, E. R. Antoniuk, G. Cheon, Y. Cui, and E. J. Reed, Machine learning-assisted discovery of solid Li-ion conducting materials, Chem. Mater. **31**, 342 (2018).

[13] W. D. Richards, L. J. Miara, Y. Wang, J. C. Kim, and G. Ceder, Interface stability in solid-state batteries, Chem. Mater. **28**, 266 (2015).

[14] C. Monroe and J. Newman, The impact of elastic deformation on deposition kinetics at lithium/polymer interfaces, J. Electrochem. Soc. **152** (2005).

[15] J. Janek and W. G. Zeier, A solid future for battery development, Nature Ener. **1**, 1 (2016).

[16] S. Ohno, T. Bernges, J. Buchheim, M. Duchardt, A.-K. Hatz, M. A. Kraft, H. Kwak, A. L. Santhosha, Z. Liu, N. Minafra, F. Tsuji, A. Sakuda, R. Schlem, S. Xiong, Z. Zhang, P. Adelhelm, H. Chen, A. Hayashi, Y. S. Jung, B. V. Lotsch, B. Roling, N. M. Vargas-Barbosa, and W. G. Zeier, How certain are the reported ionic conductivities of thiophosphate-based solid electrolytes? an interlaboratory study, ACS Energy Lett. **5**, 910 (2020).

[17] S. Ohno, A. Banik, G. F. Dewald, M. A. Kraft, T. Krauskopf, N. Minafra, P. Till, M. Weiss, and W. G. Zeier, Materials design of ionic conductors for solid state batteries, Prog. Energy **2**, 022001 (2020).

[18] A. Banik, T. Famprikis, M. Ghidiu, S. Ohno, M. A. Kraft, and W. G. Zeier, On the underestimated influence of synthetic conditions in solid ionic conductors, Chemical Science **12**, 6238 (2021).

[19] B. V. Lotsch and J. Maier, Relevance of solid electrolytes for lithium-based batteries: A realistic view, J. Electroceram. **38**, 128 (2017).

[20] M. Philipp, B. Gadermaier, P. Posch, I. Hanzu, S. Ganschow, M. Meven, D. Rettenwander, G. J. Redhammer, and H. M. R. Wilkening, The electronic conductivity of single crystalline Ga-stabilized cubic $Li_7La_3Zr_2O_{12}$: A technologically relevant parameter for all-solid-state batteries, Adv. Mater. Inter. **7**, 2000450 (2020).

[21] F. Aguesse, W. Manalastas, L. Buannic, J. M. Lopez del Amo, G. Singh, A. Llordés, and J. Kilner, Investigating the dendritic growth during full cell cycling of garnet electrolyte in direct contact with Li metal, ACS Appl. Mater. & Inter. **9**, 3808 (2017).

[22] Y. Song, L. Yang, W. Zhao, Z. Wang, Y. Zhao, Z. Wang, Q. Zhao, H. Liu, and F. Pan, Revealing the short-circuiting mechanism of garnet-based solid-state electrolyte, Adv. Energy Mater. **9**, 1900671 (2019).

[23] F. Han, A. S. Westover, J. Yue, X. Fan, F. Wang, M. Chi, D. N. Leonard, N. J. Dudney, H. Wang, and C. Wang, High electronic conductivity as the origin of lithium dendrite formation within solid electrolytes, Nature Ener. **4**, 187 (2019).

[24] An analogous degradation process due to reduction of Na^+ to Na resulting from electronic conduction has been discussed for Na-beta-alumina [94, 95].

[25] H.-K. Tian, Z. Liu, Y. Ji, and Chen, Interfacial electronic properties dictate Li dendrite growth in solid electrolytes, Chem. Mater. **31**, 7351 (2019).

[26] P. Gorai, T. Famprikis, B. S. Gill, V. Stevanović, and P. Canepa, The devil is in the defects: Electronic conductivity in solid electrolytes 10.26434/chemrxiv.13167197.v1 (2020).

[27] N. Ashcroft, *Solid State Physics* (Cengage Learning, Andover England, 1976).

[28] C. Freysoldt, B. Grabowski, T. Hickel, J. Neugebauer, G. Kresse, A. Janotti, and C. G. Van de Walle, First-principles calculations for point defects in solids, Rev. Mod. Phys. **86**, 253 (2014).

[29] J. Buckeridge, Equilibrium point defect and charge carrier concentrations in a material determined through calculation of the self-consistent fermi energy, Comp. Phys. Commun. **244**, 329 (2019).

[30] M. D. Radin and D. J. Siegel, Charge transport in lithium peroxide: relevance for rechargeable metal–air batteries, Energy Environ. Sci. **6**, 2370 (2013).

[31] J. G. Smith, J. Naruse, H. Hiramatsu, and D. J. Siegel, Intrinsic conductivity in magnesium–oxygen battery discharge products: MgO and MgO_2, Chem. Mater. **29**, 3152 (2017).

[32] H. Park, N. Kumar, M. Melander, T. Vegge, J. M. G. Lastra, and D. J. Siegel, Adiabatic and nonadiabatic charge transport in Li-S batteries, Chem. Mater. **30**, 915 (2018).

[33] P. Canepa, G. S. Gautam, D. Broberg, S.-H. Bo, and G. Ceder, Role of point defects in spinel Mg chalcogenide conductors, Chem. Mater. **29**, 9657 (2017).

[34] A. G. Squires, D. O. Scanlon, and B. J. Morgan, Native defects and their doping response in the lithium solid electrolyte $Li_7La_3Zr_2O_{12}$, Chem. Mater. **32**, 1876 (2020).

[35] S. Poncé, E. Margine, C. Verdi, and F. Giustino, EPW: Electron–phonon coupling, transport and superconducting properties using maximally localized Wannier functions, Comp. Phys. Commun. **209**, 116 (2016).

[36] S. Poncé, D. Jena, and F. Giustino, Hole mobility of strained GaN from first principles, Phys. Rev. B **100**, 085204 (2019).

[37] S. Poncé, W. Li, S. Reichardt, and F. Giustino, First-principles calculations of charge carrier mobility and conductivity in bulk semiconductors and two-dimensional materials, Rep. Prog. Phys. **83**, 036501 (2020).

[38] J. M. Frost, Calculating polaron mobility in halide perovskites, Phys. Rev. B **96**, 195202 (2017).

[39] A. M. Ganose, J. Park, A. Faghaninia, R. Woods-Robinson, K. A. Persson, and A. Jain, Efficient calculation of carrier scattering rates from first principles, Nature Communications **12**, 2222 (2021).

[40] D. O. Scanlon, A. B. Kehoe, G. W. Watson, M. O. Jones, W. I. F. David, D. J. Payne, R. G. Egdell, P. P. Edwards, and A. Walsh, Nature of the band gap and origin of the conductivity of pbo_2 revealed by theory and experiment, Phys. Rev. Lett. **107**, 246402 (2011).

[41] D. O. Scanlon, P. D. C. King, R. P. Singh, A. de la Torre, S. M. Walker, G. Balakrishnan, F. Baumberger, and C. R. A. Catlow, Controlling bulk conductivity in topological insulators: Key role of anti-site defects, Adv. Mater. **24**, 2154 (2012).

[42] C. G. V. de Walle, Hydrogen as a cause of doping in zinc oxide, Phys. Rev. Lett. **85**, 1012 (2000).

[43] A. G. Squires, J. M. Dean, and B. J. Morgan, Aliovalent doping strategies for enhancing ionic conductivity in Li_3OCl solid electrolytes: a first-principles assessment, In preparation (2021).

[44] Z. Zhu, I.-H. Chu, Z. Deng, and S. P. Ong, Role of Na^+ interstitials and dopants in enhancing the Na^+ conductivity of the cubic Na_3PS_4 superionic conductor, Chem. Mater. **27**, 8318 (2015).

[45] N. Bernstein, M. D. Johannes, and K. Hoang, Origin of the structural phase transition in $li_7la_3zr_2o_{12}$, Phys. Rev. Lett. **109**, 205702 (2012).

[46] T. Fuchs, S. P. Culver, P. Till, and W. G. Zeier, Defect-mediated conductivity enhancements in $Na_{3-x}Pn_{1-x}W_xS_4$ (Pn = P, Sb) using aliovalent substitutions, ACS Energy Lett. **5**, 146 (2019).

[47] C. Kittel, *Thermal Physics* (W. H. Freeman, San Francisco, 1980).

[48] S. B. Zhang and J. E. Northrup, Chemical potential dependence of defect formation energies in GaAs: Application to Ga self-diffusion, Phys. Rev. Lett. **67**, 2339 (1991).

[49] S. Lany and A. Zunger, Assessment of correction methods for the band-gap problem and for finite-size effects in supercell defect calculations: Case studies for zno and gaas, Phys. Rev. B **78**, 235104 (2008).

[50] S. Kim, S. N. Hood, J.-S. Park, L. D. Whalley, and A. Walsh, Quick-start guide for first-principles modelling of point defects in crystalline materials, Journal of Physics: Energy **2**, 036001 (2020).

[51] R. W. Hellwarth and I. Biaggio, Mobility of an electron in a multimode polar lattice, Phys. Rev. B **60**, 299 (1999).

[52] R. P. Feynman, Slow electrons in a polar crystal, Phys. Rev. **97**, 660 (1955).

[53] P. Y. Yu and M. Cardona, *Fundamentals of Semiconductors* (Springer Berlin Heidelberg, 2010).

[54] D. W. Davies, C. N. Savory, J. M. Frost, D. O. Scanlon, B. J. Morgan, and A. Walsh, Descriptors for electron and hole charge carriers in metal oxides, J. Phys. Chem. Lett. **11**, 438 (2019).

[55] L. D. Whalley, J. M. Frost, B. J. Morgan, and A. Walsh, Impact of nonparabolic electronic band structure on the optical and transport properties of photovoltaic materials, Phys. Rev. B **99**, 085207 (2019).

[56] For comparison, the charge carrier effective masses in semiconductors being investigated or deployed as photovoltaics which rely on mobile electronic charge carriers (e.g., $CH_3NH_3PbI_3$ or Cu_2ZnSnS_4) are typically < 1 [55].

[57] For comparison, carrier mobility in doped indium oxides used as in commercial devices as transparent conducting oxides is of the order $10\,cm^2\,V^{-1}\,s^{-1}$ to $100\,cm^2\,V^{-1}\,s^{-1}$ [96].

[58] C. J. Bradley, *The Mathematical Theory of Symmetry in Solids: Representation Theory for Point Groups and Space Groups* (Clarendon Press, Oxford New York, 2010).

[59] L. D. Whalley, effmass: An effective mass package, J. Open Source Soft. **3**, 797 (2018).

[60] P. Canepa, J. A. Dawson, G. S. Gautam, J. M. Statham, S. C. Parker, and M. S. Islam, Particle morphology and lithium segregation to surfaces of the $Li_7La_3Zr_2O_{12}$ solid electrolyte, Chem. Mater. **30**, 3019 (2018).

[61] CRC Handbook, *CRC Handbook of Chemistry and Physics, 88th Edition*, 88th ed. (CRC Press, 2007).

[62] M. Finnis, A. Lozovoi, and A. Alavi, The oxidation of NiAl: What can we learn from ab initio calculations?, Annu. Rev. Mater. Res. **35**, 167 (2005).

[63] V. Thangadurai, S. Narayanan, and D. Pinzaru, Garnet-type solid-state fast Li ion conductors for Li batteries: critical review, Chem. Soc. Rev. **43**, 4714 (2014).

[64] K. Sasaki and J. Maier, Low-temperature defect chemistry of oxides. I. general aspects and numerical calculations, J. Appl. Phys. **86**, 5422 (1999).

[65] J. Maier, Complex oxides: high temperature defect chemistry vs. low temperature defect chemistry, Phys. Chem. Chem. Phys. **5**, 2164 (2003).

[66] R. Brugge, J. Kilner, and A. Aguadero, Germanium as a donor dopant in garnet electrolytes, Sol. Stat. Ionics **337**, 154 (2019).

[67] F. Pesci, R. H. Brugge, A. K. O. Hekselman, A. Cavallaro, R. J. Chater, and A. Aguadero, Elucidating the role of dopants in the critical current density for dendrite formation in garnet electrolytes, J. Mater. Chem. A **6**, 19817 (2018).

[68] X. Liu, R. Garcia-Mendez, A. R. Lupini, Y. Cheng, Z. D. Hood, F. Han, A. Sharafi, J. C. Idrobo, N. J. Dudney, C. Wang, C. Ma, J. Sakamoto, and M. Chi, Local electronic structure variation resulting in Li 'filament' formation within solid electrolytes, Nature Mater. 10.1038/s41563-021-01019-x (2021).

[69] J. M. Dean, S. W. Coles, W. R. Saunders, A. R. McCluskey, M. J. Wolf, A. B. Walker, and B. J. Morgan, Overscreening and underscreening in solid-electrolyte grain boundary space-charge layers (2021), arXiv:2104.00623 [cond-mat.mtrl-sci].

[70] M. W. Swift, J. W. Swift, and Y. Qi, Modeling the electrical double layer at solid-state electrochemical interfaces, Nature Comp. Sci. **1**, 212 (2021).

[71] A. G. Squires, D. O. Scanlon, and B. J. Morgan, Dataset for native defects and their doping response in the lithium solid electrolyte $Li_7La_3Zr_2O_{12}$.

[72] A. G. Squires, supporting code, `github.com/alexsquires/llzo_elect_conductivity`.

[73] awaiting doi.

[74] S. P. Ong, W. D. Richards, A. Jain, G. Hautier, M. Kocher, S. Cholia, D. Gunter, V. L. Chevrier, K. A. Persson, and G. Ceder, Python materials genomics (pymatgen): A robust, open-source python library for materials analysis, Comp. Mater. Sci. **68**, 314 (2013).

[75] J. D. Hunter, Matplotlib: A 2D graphics environment, Comput. Sci. Eng. **9**, 90 (2007).

[76] W. McKinney, Data structures for statistical computing in Python, in *Proceedings of the 9th Python in Science Conference*, edited by S. van der Walt and J. Millman (2010) pp. 51 – 56.

[77] S. v. d. Walt, S. C. Colbert, and G. Varoquaux, The numpy array: A structure for efficient numerical computation, Comput. Sci. Eng. **13**, 22 (2011).

[78] P. Virtanen, , R. Gommers, T. E. Oliphant, M. Haberland, T. Reddy, D. Cournapeau, E. Burovski, P. Peterson, W. Weckesser, J. Bright, S. J. van der Walt, M. Brett, J. Wilson, K. J. Millman, N. Mayorov, A. R. J. Nelson, E. Jones, R. Kern, E. Larson, C. J. Carey, İ. Polat, Y. Feng, E. W. Moore, J. VanderPlas, D. Laxalde, J. Perktold, R. Cimrman, I. Henriksen, E. A. Quintero, C. R. Harris, A. M. Archibald, A. H. Ribeiro, F. Pedregosa, and P. van Mulbregt, SciPy 1.0: fundamental algorithms for scientific computing in Python, Nature Meth. **17**, 261 (2020).

[79] J. M. Skelton, L. A. Burton, A. J. Jackson, F. Oba, S. C. Parker, and A. Walsh, Lattice dynamics of the tin sulphides SnS_2, SnS and Sn_2S_3: vibrational spectra and thermal transport, Phys. Chem. Chem. Phys. **19**, 12452 (2017).

[80] B. J. Morgan, vasppy (2019).

[81] B. J. Morgan, vasppy: A python suite for manipulating VASP input and output, (2018), https://github.com/bjmorgan/vasppy.

[82] C. O. da Costa-Luis, tqdm: A fast, extensible progress meter for Python and CLI, J. Open Source Soft. **4**, 1277

(2019).

[83] B. J. Morgan, A. G. Squires, py-sc-fermi, `https://github.com/bjmorgan/py-sc-fermi`.

[84] G. Kresse and J. Hafner, Ab initio molecular dynamics for liquid metals, Phys. Rev. B **47**, 558 (1993).

[85] G. Kresse and J. Hafner, Ab initio molecular-dynamics simulation of the liquid-metal–amorphous-semiconductor transition in germanium, Phys. Rev. B **49**, 14251 (1994).

[86] G. Kresse and J. Furthmüller, Efficient iterative schemes for ab initio total-energy calculations using a plane-wave basis set, Phys. Rev. B **54**, 11169 (1996).

[87] P. E. Blöchl, Projector augmented-wave method, Phys. Rev. B **50**, 17953 (1994).

[88] J. Heyd, G. E. Scuseria, and M. Ernzerhof, Hybrid functionals based on a screened coulomb potential, J. Chem. Phys. **118**, 8207 (2003).

[89] A. V. Krukau, O. A. Vydrov, A. F. Izmaylov, and G. E. Scuseria, Influence of the exchange screening parameter on the performance of screened hybrid functionals, J. Chem. Phys. **125** (2006).

[90] F. D. Murnaghan, The compressibility of media under extreme pressures, Proc. Nat. Acad. Sci. **30**, 244 (1944).

[91] M. Gajdoš, K. Hummer, G. Kresse, J. Furthmüller, and F. Bechstedt, Linear optical properties in the projector-augmented wave methodology, Phys. Rev. B **73**, 045112 (2006).

[92] J. P. Perdew, A. Ruzsinszky, G. I. Csonka, O. A. Vydrov, G. E. Scuseria, L. A. Constantin, X. Zhou, and K. Burke, Restoring the density-gradient expansion for exchange in solids and surfaces, Phys. Rev. Lett. **100**, 136406 (2008).

[93] S. T. Murphy and N. D. M. Hine, Anisotropic charge screening and supercell size convergence of defect formation energies, Phys. Rev. B **87**, 094111 (2013).

[94] L. C. D. Jonghe, L. Feldman, and A. Buechele, Failure modes of na-beta alumina, Sol. Stat. Ionics **5**, 267 (1981).

[95] L. C. D. Jonghe, L. Feldman, and A. Beuchele, Slow degradation and electron conduction in sodium/beta-aluminas, J. Mater. Sci. **16**, 780 (1981).

[96] J. E. N. Swallow, B. A. D. Williamson, S. Sathasivam, M. Birkett, T. J. Featherstone, P. A. E. Murgatroyd, H. J. Edwards, Z. W. Lebens-Higgins, D. A. Duncan, M. Farnworth, P. Warren, N. Peng, T.-L. Lee, L. F. J. Piper, A. Regoutz, C. J. Carmalt, I. P. Parkin, V. R. Dhanak, D. O. Scanlon, and T. D. Veal, Resonant doping for high mobility transparent conductors: the case of Mo-doped In_2O_3, Mater. Horiz. **7**, 236 (2020).